9. T. J. Buschman, E. K. Miller, *Science* **315**, 1860–1862 (2007).
10. G. G. Gregoriou, S. J. Gotts, H. Zhou, R. Desimone, *Science* **324**, 1207–1210 (2009).
11. T. Moore, K. M. Armstrong, *Nature* **421**, 370–373 (2003).
12. B. Noudoost, T. Moore, *Nature* **474**, 372–375 (2011).
13. L. B. Ekstrom, P. R. Roelfsema, J. T. Arsenault, G. Bonmassar, W. Vanduffel, *Science* **321**, 414–417 (2008).
14. Y. Chen *et al*., *Nat. Neurosci.* **11**, 974–982 (2008).
15. K. A. Sundberg, J. F. Mitchell, J. H. Reynolds, *Neuron* **61**, 952–963 (2009).
16. K. McAlonan, J. Cavanaugh, R. H. Wurtz, *Nature* **456**, 391–394 (2008).
17. G. Purushothaman, R. Marion, K. Li, V. A. Casagrande, *Nat. Neurosci.* **15**, 905–912 (2012).
18. M. Sarter, M. E. Hasselmo, J. P. Bruno, B. Givens, *Brain Res. Brain Res. Rev.* **48**, 98–111 (2005).
19. Y. B. Saalmann, M. A. Pinsk, L. Wang, X. Li, S. Kastner, *Science* **337**, 753–756 (2012).
20. M. A. Segraves, M. E. Goldberg, *J. Neurophysiol.* **58**, 1387–1419 (1987).
21. The projection to superior colliculus arises only from deep layers (Fig. 1D), similar to that in primate FEF.
22. S. Treue, J. C. Martínez Trujillo, *Nature* **399**, 575–579 (1999).
23. T. Moore, M. Fallah, *J. Neurophysiol.* **91**, 152–162 (2004).
24. X. Xu, K. D. Roby, E. M. Callaway, *J. Comp. Neurol.* **518**, 389–404 (2010).
25. G. Fishell, B. Rudy, *Annu. Rev. Neurosci.* **34**, 535–567 (2011).
26. H. Adesnik, W. Bruns, H. Taniguchi, Z. J. Huang, M. Scanziani, *Nature* **490**, 226–231 (2012).
27. S. H. Lee *et al*., *Nature* **488**, 379–383 (2012).
28. N. R. Wilson, C. A. Runyan, F. L. Wang, M. Sur, *Nature* **488**, 343–348 (2012).
29. L. Petreanu, T. Mao, S. M. Sternson, K. Svoboda, *Nature* **457**, 1142–1145 (2009).
30. I. R. Wickersham *et al*., *Neuron* **53**, 639–647 (2007).
31. S. Lee, I. Kruglikov, Z. J. Huang, G. Fishell, B. Rudy, *Nat. Neurosci.* **16**, 1662–1670 (2013).
32. L. Madisen *et al*., *Nat. Neurosci.* **15**, 793–802 (2012).
33. Y. Fu *et al*., *Cell* **156**, 1139–1152 (2014).
34. C. K. Pfeffer, M. Xue, M. He, Z. J. Huang, M. Scanziani, *Nat. Neurosci.* **16**, 1068–1076 (2013).
35. H. J. Pi *et al*., *Nature* **503**, 521–524 (2013).
36. J. F. Mitchell, K. A. Sundberg, J. H. Reynolds, *Neuron* **55**, 131–141 (2007).
37. Based on a magnification factor of 10 μm per degree in mouse V1 (*42*), 200 μm of cortical distance corresponds to 20° of visual angle. A previous study (*26*) showed that for most neurons, the preferred size of visual stimulus was <15° in radius, and stimuli beyond this radius suppressed neuronal responses. This suggests that surround suppression for top-down modulation and bottom-up processing occur on similar spatial scales. The same inhibitory circuits could also contribute to decreased receptive field similarity and signal correlation between V1 neurons over ~200 μm (*42*).
38. J. J. Letzkus *et al*., *Nature* **480**, 331–335 (2011).
39. X. Jiang, G. Wang, A. J. Lee, R. L. Stornetta, J. J. Zhu, *Nat. Neurosci.* **16**, 210–218 (2013).
40. S. P. Mysore, E. I. Knudsen, *Nat. Neurosci.* **16**, 473–478 (2013).
41. S. Ardid, X. J. Wang, A. Compte, *J. Neurosci.* **27**, 8486–8495 (2007).
42. V. Bonin, M. H. Histed, S. Yurgenson, R. Clay Reid, *J. Neurosci.* **31**, 18506 (2011).

ACKNOWLEDGMENTS

We thank L. Pinto and Y. Zhu for help with data analysis; S. H. Lee and M. Zhao for technical assistance; Standford Neuroscience Gene Vector and Virus Core for AAV-DJ supply; K. Deisseroth, E. Callaway, B. Lim, and B. C. Weissbourd for virus and constructs; and R. Desimone, L. Wang, and M. A. Segraves for helpful discussions. This work was supported by NIH grant R01 EY018861, NSF grant 22250400-42533, a Uehara Memorial Foundation fellowship, and the Human Frontier Science Program. All primary histological, electrophysiological, and behavioral data are archived in the Department of Molecular and Cell Biology, University of California, Berkeley.

SUPPLEMENTARY MATERIALS

www.sciencemag.org/content/345/6197/660/suppl/DC1
Materials and Methods
Figs. S1 to S8
References (*43–51*)

31 March 2014; accepted 27 June 2014
10.1126/science.1254126

OCEANOGRAPHY

Centennial changes in North Pacific anoxia linked to tropical trade winds

Curtis Deutsch,[1]* William Berelson,[2] Robert Thunell,[3] Thomas Weber,[1] Caitlin Tems,[2] James McManus,[4]† John Crusius,[5] Taka Ito,[6] Timothy Baumgartner,[7] Vicente Ferreira,[7] Jacob Mey,[8,9] Alexander van Geen[8]

Climate warming is expected to reduce oxygen (O_2) supply to the ocean and expand its oxygen minimum zones (OMZs). We reconstructed variations in the extent of North Pacific anoxia since 1850 using a geochemical proxy for denitrification ($\delta^{15}N$) from multiple sediment cores. Increasing $\delta^{15}N$ since ~1990 records an expansion of anoxia, consistent with observed O_2 trends. However, this was preceded by a longer declining $\delta^{15}N$ trend that implies that the anoxic zone was shrinking for most of the 20th century. Both periods can be explained by changes in winds over the tropical Pacific that drive upwelling, biological productivity, and O_2 demand within the OMZ. If equatorial Pacific winds resume their predicted weakening trend, the ocean's largest anoxic zone will contract despite a global O_2 decline.

Below the ocean's surface, the decomposition of sinking detritus creates a layer of low-O_2 water inhospitable to many marine species (*1*). These oxygen minimum zones (OMZs) are predicted to expand with climate warming (*2*, *3*), causing a major disruption to ecosystems, especially in areas where OMZ waters impinge on coastal environments already under low-O_2 stress from natural or human causes (*4*–*6*). This putative expansion stems from two direct consequences of climate change: As the surface ocean warms, its gas solubility and density both decrease, reducing the concentration of O_2 in surface water and the rate at which that water is transported downward against a more stable stratification. The resulting decline in O_2 supply to the ocean interior is generally supported by observed trends toward lower O_2 over the past few decades, over many parts of the world's oceans (*7*), including the strong OMZs in the tropics (*8*).

The climatic response of the OMZ also depends on O_2 demand, although the factors governing those biological rates are less well understood. Earth system model simulations project large future decreases in the sinking flux of organic matter throughout the tropics (*9*), which should reduce O_2 demand in the OMZ, counteracting the loss of O_2 supply. In the eastern tropical and subtropical Pacific Ocean, the OMZ variability over the last 50 years appears to have been driven primarily by O_2 demand, which is strongly modulated by decadal climate variability (*10*, *11*). In light of that variability, the instrumental O_2 record is still sparse and short, making long-term trends in the OMZ difficult to detect or attribute especially in the most intense tropical OMZs in the Pacific and Indian oceans (*8*, *12*). The relative strength of future changes in O_2 supply versus demand in the tropical OMZ would be clearer if their long-term response to the climate warming since the industrial revolution were known.

We reconstructed changes in the OMZ of the eastern tropical northern Pacific (ETNP) over the past 150 years using a geochemical proxy for water column anoxia that is recorded in sediments (Fig. 1). At the eastern terminus of the OMZ, where thermocline waters shoal toward the productive surface layer, respiration depletes O_2 and anaerobic bacteria begin reducing nitrate (NO_3^-) to oxidize organic matter (*13*) (Fig. 1). This denitrification process preferentially removes the lighter ^{14}N isotope of N, leaving a residual NO_3^- pool enriched in heavier ^{15}N (*14*, *15*). The resulting nitrate with a high isotope ratio, $\delta^{15}N$ [$\delta^{15}N = ({}^{15}N/{}^{14}N)/R_{air} - 1) \times 1000$, where R_{air} is the N isotope ratio in air], is upwelled to the surface, where it can be transferred to plankton communities and then, via sinking particles, into sediments (*16*, *17*). In regions with complete consumption of upwelled nitrate, the $\delta^{15}N$ of particulate organic nitrogen (PON) accumulating on the sea floor closely resembles that of nitrate in waters at ~100 m (*18*). In the absence of postdepositional alteration, downcore variations in $\delta^{15}N$ provide a history of the integrated rates of denitrification and the size of the OMZ to which it is confined (*19*, *20*).

To ensure a representative history of changes in OMZ intensity, we analyzed sediment cores from three sites along the North American margin

---

[1] School of Oceanography, University of Washington, Seattle, WA, USA. [2] Department of Earth Sciences, University of Southern California, Los Angeles, CA, USA. [3] Department of Earth and Ocean Sciences, University of South Carolina, Columbia, SC, USA. [4] College of Earth, Ocean, and Atmospheric Sciences, Oregon State University, Corvallis, OR, USA. [5] U.S. Geological Survey, University of Washington School of Oceanography, Seattle, WA, USA. [6] School of Earth and Atmospheric Sciences, Georgia Institute of Technology, Atlanta, GA, USA. [7] Departamento de Oceanografía Biológica, Centro de Investigación Científica y de Educación Superior de Ensenada, Baja California, México. [8] Lamont-Doherty Earth Observatory of Columbia University, Palisades, NY, USA. [9] Department of Physical Sciences, Kingsborough Community College, City University of New York, New York, NY, USA.
***Corresponding author. E-mail: cdeutsch@uw.edu** †Present address: Department of Geosciences, University of Akron, Akron, OH, USA.

at high temporal resolution (*21*). Two sites lay within the anoxic zone off Baja California (Pescadero Slope and Soledad Basin). A third is from the Southern California Bight (Santa Monica Basin), which is >1000 km north of the anoxic zone but physically connected via the coastal undercurrent (*22*, *23*) and routinely sampled by the world's longest regional hydrographic time series, the California Cooperative Oceanic Fisheries Investigations (CalCOFI) (*6*). Sediment samples were taken at 0.8- to 3-mm intervals, yielding a nearly annual (1- to 2-year average) temporal resolution. All three sites contain distinct light and dark laminae indicating relatively undisturbed sediments and a lack of bioturbation. Measurements of δ^{15}N as a function of sediment age were determined by means of ^{210}Pb chronology (fig. S1). To minimize the potential for artifacts at the core top (*24*), we examined sediment intervals with an age greater than 1 year (*21*).

During the last 50 years, all three sediment cores reveal δ^{15}N values declining gradually by nearly 1‰ between ~1960 and the mid-1980s, followed by a more rapid increase of ~1‰ since ~1990 (Fig. 2A). Given the large differences in sediment accumulation rate and composition between sites (*25*), the coherence in δ^{15}N suggests that they have recorded primarily large-scale oceanographic changes originating in the water column rather than in the sediments. This is corroborated by an independent 18-year time series of sinking particulate matter δ^{15}N from sediment traps in Santa Barbara Basin, which exhibits an increasing trend similar to that of the sediment cores (Fig. 2A) (*21*). The timing of these decadal variations also coincides with observed changes in oxygen concentrations and nitrate deficits in hypoxic waters sampled by CalCOFI, and with changes in the volume of anoxic water in the ETNP predicted by a hindcast model for this period (*10*). These sedimentary δ^{15}N records provide a unique means to quantitatively test the mechanisms linking climate and anoxia in those model simulations.

To estimate the magnitude of changes in anoxia and denitrification implied by the sediment

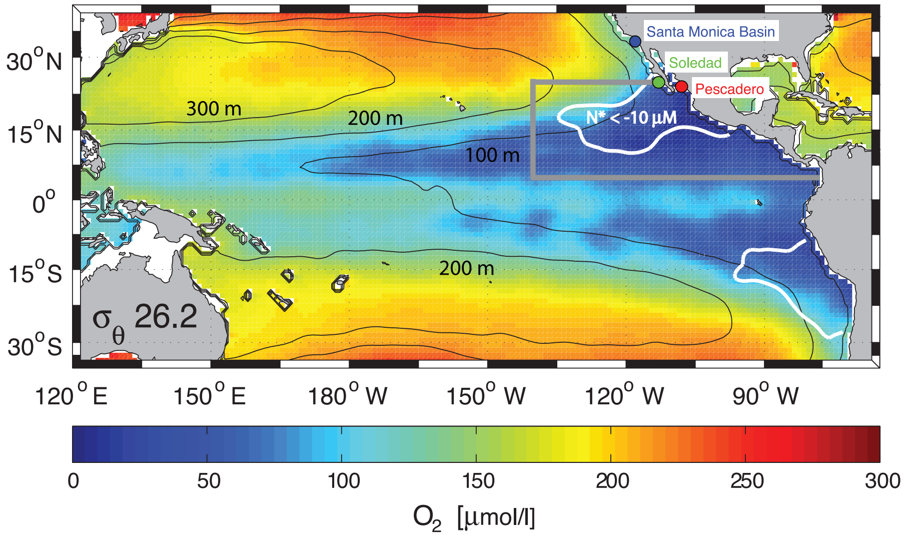

Fig. 1. Oceanographic context of study sites. Time-mean map of O_2 (colors) at a density of Central Mode Water (σ_θ = 26.2) whose mean depth (thin lines) shoals to the east, where anoxia is found off the equator in both hemispheres. Under anoxic conditions, oxidation of organic matter proceeds via denitrification, resulting in large regions (white lines) in which the primary N nutrient, nitrate (NO_3^-), falls below its expected covariation with phosphate (PO_4^{3-}) by more than 10 μM, as measured by the tracer N* (N* = [NO_3^-] – 16 × [PO_4^{3-}]). Locations of core sites are shown with circles (blue: Santa Monica Basin; red: Pescadero; green: Soledad). Gray box defines ETNP region used for analysis of modeled and observed quantities.

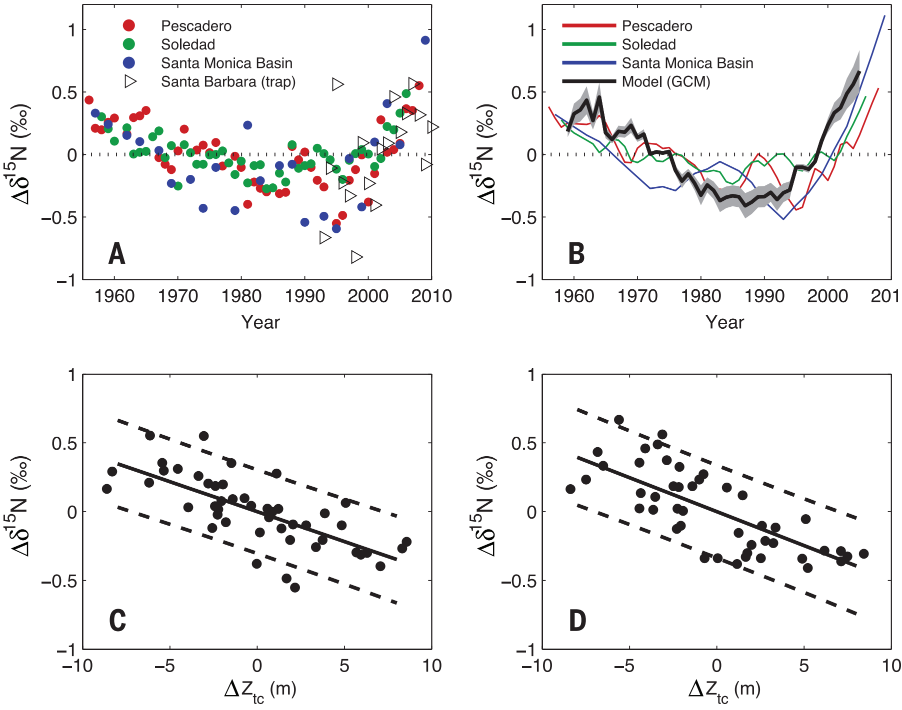

Fig. 2. Changes in sedimentary isotope ratio (δ^{15}N) and its relationship to thermocline depth (Z_{tc}) in the ETNP, from data and model simulations. (**A**) Bulk organic δ^{15}N anomalies from three sediment core sites along the North American margin (Soledad, Pescadero, Santa Monica Basin) and from a particle flux time series in Santa Barbara Basin. Each time series is plotted as a deviation from its own time-averaged value. (**B**) Variations of sinking particle flux δ^{15}N in an ocean hindcast model with an explicit N cycle, forced by reconstructed atmospheric variability. The model δ^{15}N flux is averaged over the anoxic zone (125°W to coast, 5° to 25°N). A range of values is based on uncertainty in the isotopic fractionation effect (ε_{WC} = 15 to 25‰) associated with bacterial denitrification (*15*, *21*). Thin lines are 5-year running averages of the sediment core data. (**C**) Relationship between thermocline depth (defined as the 13° isotherm) from World Ocean Database and sediment δ^{15}N in Pescadero sediment core, and (**D**) thermocline depth and particle flux δ^{15}N in model simulations. Changes in thermocline depth are averaged across the broader ETNP region (160°W to coast, 0° to 30°N). The slope of the relationship between δ^{15}N and thermocline depth in observations (–0.044 ± 0.01‰ m^{-1}; 90% confidence interval) and model simulations (–0.049 ± 0.011‰ m^{-1}) are indistinguishable.

records, we directly simulate changes in sedimentary $\delta^{15}N$ in recent decades using an ocean general circulation model (GCM). The model is expanded from previous work to include an explicit cycle of N and its isotopes (*21*). It captures the observed structure of the tropical Pacific anoxic zone, data-based rates of denitrification (*26*), and the basin-scale distribution of $\delta^{15}NO_3$ (fig. S3). In response to imposed wind and buoyancy fluxes from atmospheric reanalyses from 1959 to 2005, the N cycle simulations predict large changes in anoxic water volume and integrated denitrification rates, roughly consistent with simpler stoichiometric calculations (*10*) (fig. S4). The decadal variations in the model-predicted $\delta^{15}N$ of particulate organic N sinking into the anoxic zone are driven by the changes in denitrification and closely match the sediment proxy data in both amplitude and timing (Fig. 2B). Additional isotopic variability arising from incomplete surface nutrient utilization is much smaller in magnitude and confined to interannual time scales (fig. S4).

The sedimentary $\delta^{15}N$ data can be used to test the hypothesized mechanisms underlying recent changes in the OMZ. According to model predictions, the decadal differences in the volume of the anoxic zone are driven by respiration rates (*10*, *11*), which vary concurrently with the depth of the thermocline waters in which the OMZ is embedded. A shallower thermocline can increase the respiration rate in OMZ waters both by increasing surface photosynthetic production and sinking of organic matter, and by positioning the low-O_2 waters at depths where decomposition of the sinking particles is relatively fast. We tested this relationship using historical observations from the World Ocean Database (*27*) to estimate changes in the depth of the 13°C isotherm (fig. S5), which lies near the core of the OMZ in the eastern tropical North Pacific. Regional variations in the thermocline depth are corrected for heat uptake, and therefore attributable to changes in ocean dynamics (*21*). They are strongly correlated to sedimentary $\delta^{15}N$ (Fig. 2C), and the slope of the relationship in the data is indistinguishable from that in model simulations (Fig. 2D). The coherence between modeled particulate $\delta^{15}N$ and sediment core data suggests that the $\delta^{15}N$ records are indeed a reliable proxy for large-scale changes in the intensity of the OMZ. The strong relationship to thermocline depth independently observed in model simulations and data supports the hypothesized link to climate variability, at least on decadal time scales.

The full 150-year record of sedimentary $\delta^{15}N$ measurements reveals a declining trend throughout most of the 20th century (Fig. 3A). During most of the period of climate warming, the anoxic OMZ was evidently shrinking. To determine whether the apparent long-term contraction of anoxic volume is consistent with declining O_2 demand, we extended the thermocline depth proxy back to 1850 using Intergovernmental Panel on Climate Change (IPCC) climate model reconstructions (fig. S6). These models do not directly incorporate oceanic observations, and thus do not reproduce the phasing or magnitude of internally generated climate variability. However, they provide a self-consistent estimate of the oceanic response to observed radiative forcing, primarily by greenhouse gases. The ~10-m deepening of the thermocline over 100 years in conjunction with a ~1‰ reduction in sediment $\delta^{15}N$ is consistent with the relationship observed over decadal time scales (Fig. 3B). The relationship between North Pacific anoxia and thermocline depth diagnosed over the last several decades thus appears to characterize the dominant climatic mechanism governing anoxic zone variability for over a century.

In the tropical Pacific, high rates of surface biological productivity and the zonal structure of the underlying thermocline are both primarily governed by the strength of surface winds, which push warm surface water to the west and draw cold, nutrient-rich deep water upward along the equator in the east. The overall rate of respiration in the tropical thermocline, and its partitioning into the intense OMZ by thermocline depth fluctuations, should therefore both be closely linked to the atmospheric Walker circulation (fig. S7). Indeed, historical changes in equatorial wind stress, recorded in the zonal sea-level pressure gradient (Fig. 3C), imply a long-term weakening trend followed by a recent intensification (*28*–*30*). Both these features are reflected in thermocline depth variations and the volume of anoxia inferred from sedimentary $\delta^{15}N$. Because the oxygen content of the thermocline integrates respiration rates over multiyear residence time of regional water masses, wind and thermocline fluctuations of shorter durations are naturally filtered out of the sediment record, leaving decadal and longer time scales (*31*). The trends in the Pacific OMZ inferred from our $\delta^{15}N$ records originate from slowly varying strength of the tropical Walker circulation and its effect on O_2 demand, rather than changes in O_2 supply due to gas solubility and thermocline ventilation. Given the mechanistic link between equatorial wind stress and the extent of anoxia, decadal to centennial variations in the sediment $\delta^{15}N$ may provide a valuable new proxy for variations in equatorial Pacific winds and upwelling at those time scales.

Our findings demonstrate that the contemporary anoxic zone of the ETNP is currently not larger than it has been in the past 150 years, and thus cast doubt on the view that the recent expansion of the tropical Pacific OMZ is a reflection of global ocean deoxygenation driven by climate warming (*8*). This expansion coincides with a period of surface cooling (fig. S8) (*32*) and thermocline shoaling in the eastern tropical Pacific that runs counter to the prevailing climate-warming trend and partly accounts for the hiatus in global surface warming (*33*). It is therefore a likely manifestation of the ocean's pervasive low-frequency variability, rather than a response to rising greenhouse gases. Instead, the dominant influence of anthropogenic climate warming on tropical Pacific oxygen over the last 150 years has been the weakening of the easterly trade winds and its effect on respiratory O_2 demand. The resumption

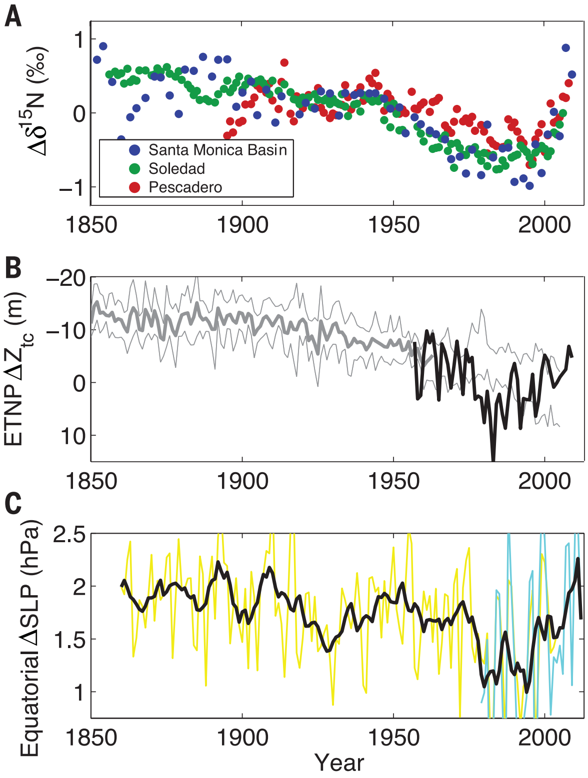

Fig. 3. Centennial changes in Pacific OMZ denitrification and its climatic forcing. (**A**) Sedimentary $\delta^{15}N$ from coring sites, extended back to 1850. (**B**) Trends in depth of the thermocline (13°C isotherm) in the ETNP from a database of historical temperature profiles (*27*) since 1955 (bold line) and from IPCC coupled climate model runs (gray line). The mean deepening across 19 individual model runs represents the response to historical radiative forcing, predominantly from greenhouse gases. The standard deviation reflects the intermodel spread as well as unforced variability, which is not in phase between models and observations. (**C**) East-west difference in sea-level pressure (ΔSLP) across the equatorial Pacific (5°N to 5°S) based on historical reconstructions (HadSLP, yellow line) and atmospheric reanalysis (ECMWF ERA40, cyan line) (*39*, *40*). Black line is 10-year running mean of the average of the data sets. The ΔSLP is a measure of trade wind strength, with larger values indicating stronger easterly surface winds.

of Pacific trade wind slackening predicted under future climate warming should extend the 20th-century contraction of the OMZ into this century. This wind-driven forcing may eventually be overwhelmed by the stratification-driven deoxygenation of the ocean as a whole, as proxies of anoxia from Pleistocene sediments point to a larger tropical OMZ and greater N loss during warm climates (*19*, *34*, *35*). The relative influence of these effects and the time scales over which they operate on the tropical OMZ remain unknown.

The predominant 20th-century contraction of the North Pacific OMZ has important implications for the basin's N cycle. Over centennial time scales, the slowing pace of N loss would have reduced the NO_3^- deficit relative to plankton PO_4^{3-} requirements throughout surface waters of the N-limited North Pacific. Recent isotopic analysis of skeleton material from deep-sea corals near Hawaii also exhibit a decreasing trend over this time period, which has been interpreted as a signal of increasing N inputs from N_2 fixation (*36*). However, because isotopic and stoichiometric signals of denitrification are transported from the anoxic zone into the subtropical gyre (*37*), the reported coral trends may originate partly from the OMZ. Any remaining signal attributable to N_2 fixation would imply that the ecological niche of diazotrophs in the central gyre is uncoupled from the major N loss in the OMZ (*38*), and that a substantial imbalance of the Pacific N budget has persisted over the 20th century.

REFERENCES AND NOTES

1. R. Vaquer-Sunyer, C. M. Duarte, *Proc. Natl. Acad. Sci. U.S.A.* **105**, 15452–15457 (2008).
2. L. Bopp, C. Le Quere, M. Heimann, A. C. Manning, P. Monfray, *Global Biogeochem. Cycles* **16**, 6-1–6-13 (2002).
3. R. J. Matear, A. C. Hirst, *Global Biogeochem. Cycles* **17**, 1125 (2003).
4. F. Chan *et al.*, *Science* **319**, 920 (2008).
5. R. J. Diaz, *J. Environ. Qual.* **30**, 275–281 (2001).
6. J. A. Koslow, J. Couture, *Nature* **502**, 163–164 (2013).
7. R. E. Keeling, A. Körtzinger, N. Gruber, *Annu. Rev. Mar. Sci.* **2**, 199–229 (2010).
8. L. Stramma, G. C. Johnson, J. Sprintall, V. Mohrholz, *Science* **320**, 655–658 (2008).
9. L. Bopp *et al.*, *Biogeosciences* **10**, 6225–6245 (2013).
10. C. Deutsch, H. Brix, T. Ito, H. Frenzel, L. Thompson, *Science* **333**, 336–339 (2011).
11. T. Ito, C. Deutsch, *Global Biogeochem. Cycles* **27**, 1119–1128 (2013).
12. S. McClatchie, R. Goericke, R. Cosgrove, G. Auad, R. Vetter, *Geophys. Res. Lett.* **37**, L19602 (2010).
13. L. A. Codispoti, J. P. Christensen, *Mar. Chem.* **16**, 277–300 (1985).
14. J. A. Brandes, A. H. Devol, T. Yoshinari, D. A. Jayakumar, S. W. A. Naqvi, *Limnol. Oceanogr.* **43**, 1680–1689 (1998).
15. K. Kritee *et al.*, *Geochim. Cosmochim. Acta* **92**, 243–259 (2012).
16. M. A. Altabet, *J. Geophys. Res.* **94**, 12771 (1989).
17. D. M. Sigman, K. L. Casciotti, in *Encyclopedia of Ocean Sciences*, J. H. Steele, K. K. Turekian, S. A. Thorpe, Eds. (Academic Press, London, 2001), vol. 4, pp. 1884–1894.
18. R. C. Thunell, D. M. Sigman, F. Muller-Karger, Y. Astor, R. Varela, *Global Biogeochem. Cycles* **18**, GB3001 (2004).
19. R. S. Ganeshram, T. F. Pedersen, S. E. Calvert, G. W. McNeill, M. R. Fontugne, *Paleoceanography* **15**, 361–376 (2000).
20. M. A. Altabet, M. J. Higginson, D. W. Murray, *Nature* **415**, 159–162 (2002).
21. See supplementary materials on *Science* Online.
22. C. G. Castro, F. P. Chavez, C. A. Collins, *Global Biogeochem. Cycles* **15**, 819–830 (2001).
23. S. S. Kienast, S. E. Calvert, T. F. Pedersen, *Paleoceanography* **17**, 7-1–7-17 (2002).
24. M. F. Lehmann, S. M. Bernasconi, A. Barbieri, J. A. McKenzie, *Geochim. Cosmochim. Acta* **66**, 3573–3584 (2002).
25. M. G. Prokopenko *et al.*, *Earth Planet. Sci. Lett.* **242**, 186–204 (2006).
26. T. DeVries, C. Deutsch, F. Primeau, B. X. Chang, A. H. Devol, *Nat. Geosci.* **5**, 547–550 (2012).
27. J. I. Antonov, *et al.*, in *NOAA Atlas NESDros. Inf. Serv. 66* (U.S. Government Printing Office, Washington, DC, 2010).
28. G. A. Vecchi *et al.*, *Nature* **441**, 73–76 (2006).
29. H. Tokinaga, S.-P. Xie, C. Deser, Y. Kosaka, Y. M. Okumura, *Nature* **491**, 439–443 (2012).
30. M. A. Merrifield, *J. Clim.* **24**, 4126–4138 (2011).
31. T. Ito, C. Deutsch, *Geophys. Res. Lett.* **37**, L03601 (2010).
32. T. M. Smith, R. W. Reynolds, T. C. Peterson, J. Lawrimore, *J. Clim.* **21**, 2283–2296 (2008).
33. M. H. England *et al.*, *Nature Clim. Change* **4**, 222–227 (2014).
34. A. van Geen *et al.*, *Paleoceanography* **18**, 1098 (2003).
35. S. L. Jaccard, E. D. Galbraith, *Nat. Geosci.* **5**, 151–156 (2012).
36. O. A. Sherwood, T. P. Guilderson, F. C. Batista, J. T. Schiff, M. D. McCarthy, *Nature* **505**, 78–81 (2014).
37. D. M. Sigman, P. J. DiFiore, M. P. Hain, C. Deutsch, D. M. Karl, *Geophys. Res. Lett.* **36**, L08605 (2009).
38. T. Weber, C. Deutsch, *Proc. Natl. Acad. Sci. U.S.A.* **111**, 8741–8746 (2014).
39. R. Allan, T. Ansell, *J. Clim.* **19**, 5816–5842 (2006).
40. S. M. Uppala *et al.*, *Q. J. R. Meteorol. Soc.* **131**, 2961 (2005).

ACKNOWLEDGMENTS

This work was supported by grants from the National Science Foundation (OCE-0851483 to C.D.; OCE-1242313 to T.I.; OCE-0727123 to W.B.; OCE-0624777 to J.M.), by the Gordon and Betty Moore Foundation through Grant GBMF3775 to C.D., and by the U.S. Geological Survey Coastal and Marine Geology Program (J.C.). A grant from the Climate Center of Lamont-Doherty Earth Observatory (LDEO) contributed to the collection and dating of the Soledad Basin core. This is LDEO contribution number 7812.

SUPPLEMENTARY MATERIALS

www.sciencemag.org/content/345/6197/665/suppl/DC1
Materials and Methods
Figs. S1 to S8
References

17 February 2014; accepted 1 July 2014
10.1126/science.1252332

ARTIFICIAL BRAINS

A million spiking-neuron integrated circuit with a scalable communication network and interface

Paul A. Merolla,[1*] **John V. Arthur,**[1*] **Rodrigo Alvarez-Icaza,**[1*] **Andrew S. Cassidy,**[1*] **Jun Sawada,**[2*] **Filipp Akopyan,**[1*] **Bryan L. Jackson,**[1*] **Nabil Imam,**[3] **Chen Guo,**[4] **Yutaka Nakamura,**[5] **Bernard Brezzo,**[6] **Ivan Vo,**[2] **Steven K. Esser,**[1] **Rathinakumar Appuswamy,**[1] **Brian Taba,**[1] **Arnon Amir,**[1] **Myron D. Flickner,**[1] **William P. Risk,**[1] **Rajit Manohar,**[7] **Dharmendra S. Modha**[1]†

Inspired by the brain's structure, we have developed an efficient, scalable, and flexible non–von Neumann architecture that leverages contemporary silicon technology. To demonstrate, we built a 5.4-billion-transistor chip with 4096 neurosynaptic cores interconnected via an intrachip network that integrates 1 million programmable spiking neurons and 256 million configurable synapses. Chips can be tiled in two dimensions via an interchip communication interface, seamlessly scaling the architecture to a cortexlike sheet of arbitrary size. The architecture is well suited to many applications that use complex neural networks in real time, for example, multiobject detection and classification. With 400-pixel-by-240-pixel video input at 30 frames per second, the chip consumes 63 milliwatts.

A long-standing dream (*1*, *2*) has been to harness neuroscientific insights to build a versatile computer that is efficient in terms of energy and space, homogeneously scalable to large networks of neurons and synapses, and flexible enough to run complex behavioral models of the neocortex (*3*, *4*) as well as networks inspired by neural architectures (*5*).

No such computer exists today. The von Neumann architecture is fundamentally inefficient and nonscalable for representing massively interconnected neural networks (Fig. 1) with respect to computation, memory, and communication (Fig. 1B). Mixed analog-digital neuromorphic approaches have built large-scale systems (*6*–*8*) to emulate neurobiology by using custom computational elements, for example, silicon neurons (*9*, *10*), winner-take-all circuits (*11*), and sensory circuits (*12*). We have found that a multiplexed digital implementation of spiking neurons is more efficient than previous designs (supplementary section S3) and enables one-to-one correspondence between software and hardware (supplementary

---

[1]IBM Research–Almaden, 650 Harry Road, San Jose, CA 95120, USA. [2]IBM Research–Austin, 11501 Burnet Road, Austin, TX 78758, USA. [3]Cornell University, 358 Upson Hall, Ithaca, NY 14853 USA. [4]IBM Engineering and Technology Services, San Jose Design Center, 650 Harry Road, San Jose, CA 95120, USA. [5]IBM Research–Tokyo, Nippon Building Fund Toyosu Canal Front Building, 5-6-52 Toyosu, Koto-ku Tokyo 135-8511, Japan. [6]IBM T. J. Watson Research Center, 101 Kitchawan Road, Yorktown Heights, NY 10598, USA. [7]Cornell Tech, 111 Eighth Avenue No. 302, New York, NY 10011, USA.
*These authors contributed equally to this work. **†Corresponding author. E-mail: dmodha@us.ibm.com**

www.sciencemag.org/345/6197/665/suppl/DC1

Supplementary Materials for

Centennial changes in North Pacific anoxia linked to tropical trade winds

Curtis Deutsch,* William Berelson, Robert Thunell, Tom Weber, Caitlin Tems, James McManus, John Crusius, Taka Ito, Timothy Baumgartner, Vicente Ferreira, Jacob Mey, Alexander van Geen

*Corresponding author. E-mail: cdeutsch@uw.edu

Published 8 August 2014, *Science* **345**, 665 (2014)
DOI: 10.1126/science.1252332

This PDF file includes:

Materials and Methods
Figs. S1 to S8
References

Materials and Methods

Sediment Cores

We collected high-resolution time series of $\delta^{15}N$ from bulk organic matter (Fig. S1) at 3 sediment core sites within and near the anoxic zone of the ETNP: the Pescadero Slope (24°17'N, 108°12'W; 600 m bottom depth), Soledad Basin (25°13'N, 112°43'W; 540 m) off the coast of Baja California, and Santa Monica Basin (SMB, 33° 50.2' N, 119° 01.7' W, 892 m) off Southern California. Coring was done in 2007 (Soledad), 2009 (Pescadero), and 2011 (Santa Monica Basin).

Alternations in sediment color and the presence of mm-scale coccolith layers indicate that low O_2 concentrations at the bottom of Soledad Basin inhibit bioturbation of the sediment by benthic macrofauna (Soutar, 1971). A radiocarbon-dated piston core collected in 1999 shows bioturbation has not degraded the potential resolution of sediment records from Soledad Basin spanning the past 10 kyr [*van Geen et al.*, 2003]. The Soledad Basin nitrogen isotope record is based on two subcores obtained from a single Soutar box core extruded at 0.3-0.5 cm intervals to a depth of 45 cm on board B/O *Francisco de Ulloa* in June 2007. Overlap between the upper 15 cm of one of the subcores with the second subcore was established on the basis of Ca and Fe analysis of freeze-dried sediment by X-ray fluorescence. The Pescadero and Santa Monica cores analyzed for this study were also finely laminated as confirmed by X-ray analysis (Tems, unpublished and [*Christensen et al.*, 1994]). The Pescadero multi-core was split and sampled at 0.3 cm resolution and the Santa Monica multi-core was extruded at 0.08 cm intervals. Sediments were dried, ground and sub-sampled for ^{15}N and solid phase.

The nitrogen isotope composition of bulk organic matter in Soledad Basin sediment to a depth of 45 cm was determined at the University of South Carolina using a Carlo Erba elemental analyzer interfaced with a VG Optima Stable Isotope Ratio Mass Spectrometer. Urea ($\delta^{15}N = 0.10$ ‰) was used as a working standard. Samples and standards were combusted at 1020 °C, with standards spaced approximately every 10 samples. The sediment nitrogen isotope data are reported relative to atmospheric N_2 and have a reproducibility of better than 0.1% 1SD. Sediment $\delta^{15}N$ records from Pescadero and Santa Monica were analyzed on ground sediment splits, packaged in tin cups and measured by IRMS at the UC Davis Stable Isotope Lab.

The sediment age model is based on the radioisotope ^{210}Pb (half-life 22.3 years). The activity of ^{210}Pb in the Soledad core was determined at the US Geological Survey (Woods Hole) on 5-10 g of dried, disaggregated sediment. Samples were sealed in vials and stored for at least 21 days to allow for the in-growth of ^{222}Ra and ^{214}Pb. Samples were counted for 2-5 d using a Princeton Gamma-Tech Ge well detector (Princeton, NJ), detecting the 46.3 keV ^{210}Pb peak. Detector efficiencies were determined by counting standards in the same vials, and filled to the same vial height, as the samples, including EPA standard pitchblend ore and SLOSH III standard (Olsen, 1979). The ^{210}Pb was analyzed on Pescadero and Santa Monica cores in a similar fashion, also using gamma spectroscopy on dried sediment. Pescadero sediments were analyzed at Oregon State University; SMB cores were analyzed at USC.

Sediment ages were determined by dividing the cumulative mass at a given depth by the mass accumulation rate. The cumulative mass of sediment above each depth interval was calculated from salt-corrected porosity measurements. Assuming the ^{210}Pb activity of freshly deposited sediment is assumed to be constant over time, mass accumulation rates were estimated from the excess ^{210}Pb profiles fitted to an exponential decay equation using integrated mass as the independent variable. The accumulation rate in Soledad Basin is 88±11 mg cm^{-2} yr^{-1}, based on 28 measurements in the upper 25 cm of the core as well as 3 measurements at 70-72 cm depth. The accumulation rate in the Pescadero core is 77±8 mg cm^{-2} yr^{-1}. The accumulation rate used for the Santa Monica Basin core is the average value (16±2 mg cm^{-2} yr^{-1}) obtained from cores collected and analyzed by Tems et al. (in prep) merged with data from cores analyzed and summarized in Christensen et al. (1994).

Sediment Trap Time Series

A time series sediment trapping study was initiated in the center of Santa Barbara Basin (34° 14' N, 102° 02' W, trap depth 500 m) in August 1993. Two-week-long samples have been collected continuously at this site since that time. Nitrogen isotope analyses of bulk sediment material from samples collected from 1993 through 2010 were performed at the University of South Carolina following the procedure described in the previous section. Flux weighted annual average δ^{15}N values were calculated for each year.

The trend in the Santa Barbara Basin particle flux δ^{15}N (0.04±0.03 ‰/yr; 95% C.I.) is within the range of trends determined for the same period among the sediment cores (0.02 - 0.10 ‰/yr). It is lower than for the nearest sediment core, in Santa Monica Basin (0.10±0.05 ‰/yr). This difference in trend is due to the most recent, coretop data points; prior to 2007 the sediment trend (0.05±0.03 ‰/yr) is nearly identical to that of the particle flux time series. The slightly elevated values at the coretop are consistent with a transient diagenetic imprint [Lehmann et al., 2002]. However, it could also reflect a short-term change in water mass composition in the distinct basins (Santa Barbara versus Santa Monica) from which upwelling occurs in the Southern California Bight. On decadal time scales, the similarity of trends in particle flux data and subsurface sediments at all sites provides strong evidence that the latter signals originate in the water column, with minimal downcore diagenetic alteration.

Ocean Biogeochemical Model

A global biogeochemical model is used to simulate time-dependent cycles of phosphorus (P), dissolved oxygen (O_2), and nitrogen (N).

The transport of each compound by the general circulation is computed offline from a global configuration of the GFDL isopycnal ocean model (HIM/GOLD). The vertical resolution includes 2 mixed layers, 2 buffer layers, and 45 isopycnal layers with constant nominal potential densities referenced to 2000 db. The density intervals are chosen to provide the highest resolution in the thermocline. The horizontal grid (1 degree latitude and longitude, 0.5 degrees latitude in the tropics), is designed to better resolve tropical currents that influence the structure of low-O_2 zones. In addition to advective transport, constant isopycnal and diapycnal diffusivities of 1000 m^2/s and $2x10^{-5}$ m^2/s are applied to tracers. Circulation variability is forced by changes in surface winds and buoyancy fluxes from NCEP reanalysis (CORE-2) from 1959-2005 [*Large and Yeager*, 2004]. Fresh water fluxes are applied together with a restoring of sea surface salinity with a variable time scale of 0.5 m/day.

The cycles of P (PO_4^{3-} and dissolved organic phosphorus, DOP), and dissolved O_2 are adapted from the OCMIP protocol, and implemented in the isopycnal circulation as described by [*Deutsch et al.*, 2006]. A nitrogen cycle has been added, with tracers for NO_3^-, DON and their rare isotopes, $^{15}NO_3^-$, $DO^{15}N$. The uptake, export and remineralization of N is linked to that of P by a stoichiometric ratio. Upon complete utilization of O_2, further oxidant demands are met through NO_3^- consumption, representing the net effect of water-column denitrificiation and anammox. This process is accompanied by a strong isotopic fractionation elevating the $\delta^{15}N$ of the remaining NO_3^- pool of the anoxic zone. A suite of three simulations with different enrichment factors (ε_{WC} = 15, 20, 25‰) is used to account for uncertainty in this fractionation effect [*Kritee et al.*, 2012].

The simulated loss of NO_3^- from bottom water via benthic denitrification is parameterized according to the diagenesis model of [*Middelburg et al.*, 1996]. Sedimentary denitrification is assumed to exert no effective fractionation ($\varepsilon_B = 0$), due to the complete local consumption of sediment porewater NO_3^-[*Brandes and Devol*, 2002]. Nitrogen fixation is parameterized as a source of NO_3^- with a constant rate of 1mmol/m^3/yr in all oligotrophic surface waters (<75m) warmer than 15°C and with [PO_4^{3-}] lower than 0.15μM, yielding a global rate of ~100TgN/yr. Newly fixed NO_3^- is assumed to derive from an isotopically light dissolved N_2 pool with no fractionation ($\varepsilon_{Nfix} = 0$), and thus lowers $\delta^{15}NO_3^-$ in surface waters. Little N_2-fixation occurs directly above the suboxic zone of the ETNP, so its contribution to the isotopic composition of sinking particles is negligible in this region.

In our primary simulations (Fig. 2), surface NO_3^- assimilation by phytoplankton is assumed to proceed with no isotopic fractionation (ε_{assim}=0). Although a weak fractionation is generally observed, this only impacts the isotopic composition of the sinking flux in regions of incomplete nutrient utilization. Because our model estimates organic matter export by restoring nutrients toward observations over a 90 day time scale, it has a tendency to underestimate surface nutrient utilization. This amplifies the assimilation fractionation effect in our ETNP study region, where climatological observations indicate near-complete NO_3^- drawdown. Therefore, the model better reproduces the observed correspondence between thermocline $\delta^{15}NO_3$ and sinking particles [*Altabet et al.*, 1999] when this fractionation is neglected. We tested the sensitivity of our findings to this assumption by repeating the suite of isotopic simulations with ε_{assim} = 5‰ (results discussed below).

For computational efficiency, we ran the model for the Pacific basin only, while restoring toward observed climatological nutrient and O_2 fields [*Garcia et al.*, 2006] in the Southern Ocean (at 56°S) and along the western boundary with the Indian Ocean. Nitrate is supplied across the boundaries with mean-ocean isotopic composition of 5‰. The biogeochemical model is integrated for 600 years under climatological forcing before the hindcast simulation with variable circulation begins.

The model reproduces the time-mean spatial extent and thickness of ETNP suboxic waters (Fig. S3a-b), with greater accuracy than any of the Earth System Models in the most recent IPCC Climate Model Intercomparison Project (CMIP5). The simulated large-scale patterns of $N^*=[NO_3^-]-16[PO_4^{3-}]$ and $\delta^{15}NO_3$ throughout the North Pacific Ocean, and their profiles within the suboxic water-column are also broadly consistent with observational constraints [*Garcia et al.*, 2006][*DeVries et al.*, 2012]. A distinct N* minimum and $\delta^{15}NO_3$ maximum are centered in the suboxic waters just south of Baja California, most pronounced between 200-500m depth (Fig. S3c-h). Isotopically enriched NO_3^- is then transmitted to the surface ocean by upwelling and incorporated into sinking particles (Fig. S3i-j).

The structure of the anoxic zone (here taken as O_2<5 uM), and the spatially integrated rates of denitrification within it show large decadal variations (Fig. S4a-b), recorded as a decadal fluctuation of amplitude ~1‰ in particulate $\delta^{15}N$ (Fig. 4c). The magnitude and timing of this fluctuation is unchanged between simulations with and without isotopic fractionation during assimilation, indicating that observed changes over these timescales result from denitrification rather than nutrient utilization. However, the case with ε_{assim}=5‰ exhibits a larger degree of interannual variability than ε_{assim}=0, stemming from short-term variations in upwelling strength and nutrient utilization – a mechanism that potentially explains some of the high frequency variability in our sediment $\delta^{15}N$ reconstructions (Fig. 4c).

Climate Data

Ocean Temperature

The depth of the 13° isotherm, which passes through the core of the OMZ, has been suggested as a proxy for respiration rate because it reflects both the upwelling of nutrients and the relative rates of particle decomposition. We estimated changes in thermocline depth from the World Ocean Database of historical temperature data [*Antonov*, 2010]. Monthly mean temperature profiles were interpolated to find the depth of 13° water on a 1° longitude x 1° latitude grid. Anomalies in depth were computed by subtracting off the long-term mean. Spatial patterns of decadal depth anomalies are shown in Figure S5, along with the number of years containing data in each decade.

Over time scales of decades to centuries, isotherms can undergo deepening due to ocean heat uptake that is not related to upwelling rates or the depth of low-O_2 water, and thus not of direct consequence for respiration rates. To account for this, we consider temperature anomalies (T) to have 2 components, one due to changes in ocean circulation (T_{circ}) and another due to ocean heat uptake (T_{ohu}):

$$T = T_{circ} + T_{ohu}$$

A wide variety of changes in ocean circulation will yield temperature anomalies (T_{circ}), and these would pertain in a steady climate with no gain or loss of total heat content. In a warming climate, an additional anomaly (T_{ohu}) will be due to ocean heat uptake, which would be present even in a perfectly steady circulation. On a global basis, the average T_{ohu} of the upper ocean has been estimated to be a few tenths of a degree [*Levitus et al.*, 2009], and is thus much smaller than typical interannual fluctuations in T, most of which are presumed due to ocean dynamics.

To estimate the contribution of T_{ohu} to observed temperature anomalies, we assume a close correspondence between the oceanic uptake of heat anomalies, and its uptake chloroflourocarbons (CFCs). Both have been steadily rising in the atmosphere through most of the 20th century, while being transferred to the surface ocean mixed layer with an equilibration timescale of order months, before circulating into the ocean interior. Thus, we assume that T_{ohu} should have a global inventory (ΣT_{ohu}) similar to the global inventory of CFC partial pressure (ΣpCFC; we use partial pressure because it does not depend on temperature, while CFC concentration does). Since both tracers are transported into the ocean interior with the mean flow, their patterns should also be similar. Therefore, we estimate T_{ohu} by scaling the known spatial distribution of pCFC:

$$T_{ohu}(x,y,z,t) = pCFC(x,y,z,t) * \{\Sigma T_{ohu}(t)/\Sigma pCFC(t)\}$$

Ocean CFCs have been widely measured, and their time-dependent distributions commonly modeled. We estimate the time-dependent pattern of temperature anomalies due to ocean heat uptake from results of the Simple Ocean Data Assimilation (SODA) model [*Carton and Giese*, 2008], in which both quantities are computed in a self-consistent way that minimizes data misfits. In the ETNP, over decadal time scales, the effect of ocean heat uptake on thermocline depth is small (~1m), relative to the large fluctuations in thermocline depth (>10m). If this were not the case, the thermocline could not be shoaling in recent decades. By this estimate, over the last half of the 20th century, climate warming accounts for ~3-4 m of deepening of the 13° isotherm.

Sea Level Pressure and Sea Surface Temperature

The sea level pressure difference between the eastern and western equatorial Pacific has been used as a proxy for surface trade wind strength, because of the close dynamical connection between the variables, and because SLP provides a more consistent historical time series [*Vecchi et al*., 2006]. We use the Hadley Center's reconstruction of historical SLP changes from ship-based measurements globally gridded at monthly intervals from 1871–2003 [*Allan and Ansell*, 2006]. The observational data is supplemented by atmospheric reanalysis from the ECMWF ERA40 for the period from 1981-2010. The two data sets agree very well in the overlapping time period. Following [*Vecchi et al*., 2006], each dataset is used to compute a large-scale tropical SLP gradient (ΔSLP) between the central/east Pacific (160° W–80° W) and the west Pacific/Indian Ocean (80° E–160° E). The index is computed with SLP anomalies from monthly climatology and averaged over grid cells within 5° latitude of the equator.

Trends in Sea Surface Temperature (SST) over the period of apparent OMZ expansion are evaluated using two datasets – the Hadley Center's HadSST version 2 [*Rayner et al.*, 2003] and NOAA's extended reconstructed SST product [*Smith et al.*, 2008] (Fig. S7). Monthly anomalies relative to the climatological seasonal cycle are used to determine the trend at each point. Both data sets show similar patterns and magnitudes of cooling in the Eastern Tropical Pacific.

Climate Models

To extend the estimates of thermocline depth prior to the instrumental record, we use output from coupled climate model simulations conducted for the IPCC's fourth assessment report (AR4). A total of 19 model simulations (Fig. S6), were run with 8 climate models (GFDL (2 versions), IPSL, GISS (2 versions), NCAR, MPI, Hadley), all under the same radiative forcing, from a combination of greenhouse gases (CO_2, N_2O, CH_4, and CFCs), and volcanic and anthropogenic aerosols. In each model, we calculate the mean depth of the 13° C isotherm in the ETNP, as done for the observations (see above). The models also confirm that the depth of the thermocline throughout most of the Eastern Tropical Pacific (including the anoxic zone region), are closely connected to equatorial wind stress (Fig. S8).

Supporting Figure Legends

Figure S1. Excess ^{210}Pb as a function of cumulative mass from A) Pescadero, and B) Soledad sediment cores.

Figure S2. Sedimentary bulk organic δ^{15}N from 3 sites along the North American margin: A) Santa Monica Basin, B) Soledad, and C) Pescadero. Sediment records from Santa Monica Basin are overlaid by measured δ^{15}N of sinking particle flux (triangles) from sediment traps deployed in the nearby Santa Barbara Basin from 1993-2010. Deviations from the long-term average at each site were used in Figure 1.

Figure S3. Simulated time-mean (1959-2005) geochemical distributions, and comparison to observations. **A** Thickness (in meters) of Eastern North Pacific suboxic zone (O_2<5μM). **B** Observed thickness computed from monthly World Ocean Atlas climatology, corrected following Bianchi et al. 2011. **C** Simulated nitrate deficit (N* = $[NO_3^-] - 16[PO_4^{3-}]$) of thermocline waters in the depth interval of peak suboxic area (300-500m); **D** Observed N* computed from nutrient climatologies. **E** Simulated (black line) and observed (red dots) N* profiles averaged over region with suboxic thickness greater than 100m. **F** Simulated $\delta^{15}NO_3^-$ in shallow thermocline (100-300m); **G** Observed $\delta^{15}NO_3^-$ from data compilation of Rafter et al, 2012. **G** Simulated (black line) and observed (red dots) $\delta^{15}NO_3^-$ profiles, using the same averaging region as **E**. **H&I** $\delta^{15}N$ of sinking particles in simulations with isotopic enrichment factors for NO_3^- assimilation (ε_{assim}) of 0 and 5‰ respectively.

Figure S4. Time series of anoxic volume (**A**) and water column denitrification rate (**B**) in N cycle hindcast simulations, integrated over the Eastern Tropical North Pacific region. **C** Time series of sinking particulate $\delta^{15}N$ averaged over this region in simulations with isotopic enrichment factors for NO_3^- assimilation (ε_{assim}) of 0 and 5‰.

Figure S5. Decadal anomalies in thermocline depth, from 2009 World Ocean Database [*Antonov*, 2010]. The depth of the 13°C isotherm is taken as an index of the depth of suboxic water masses. It is estimated by linear interpolation of monthly mean temperature profiles on a 1° x 1° lat/lon grid. The data density is shown as the number of years in each decade for which at least one hydrocast exists. Temperature profiles are corrected for ocean heat uptake using CFC partial pressures from the Simple Ocean Data Assimilation product [*Carton and Giese*, 2008], as described above.

Figure S6. Trends in depth of 13°C isotherm in the Eastern Tropical North Pacific, from coupled climate model output. Models runs are 20th century climate reconstructions from the IPCC AR4, and were run under historical radiative forcings, most importantly from greenhouse gases (GHGs). Trends in thermocline (13°C isotherm) are the response to climate warming. Climate models without GHG forcings (not shown) exhibit no deepening trend.

Figure S7. Correlation coefficient between equatorial wind stress and thermocline depth from 1850-2005, in Earth System Models. Annual wind stress is averaged over an equatorial band (3°S-3°N) in the central Pacific (160°E-120°W), and regressed against local changes in the depth of the 13°C isotherm, which are smoothed with a 7-year boxcar average. Positive correlations indicate a deeper thermocline when winds are weaker.

Figure S8. Trends in sea surface temperature from 1990-2010 in degrees C per decade. Trends are evaluated using monthly temperature anomalies at each grid cell. Two reconstructions of SST – Hadley center [*Rayner et al.*, 2003] and NOAA's extended reconstructed SST product [*Smith et al.*, 2008] - show similar trend patterns. Over these decades during which anoxic zone has grown, cooling predominates in much of the eastern tropical Pacific, especially in the central equatorial Pacific where upwelling is most pronounced.

Supporting References

Allan, R., and T. Ansell (2006), A new globally complete monthly historical gridded mean sea level pressure dataset (HadSLP2): 1850-2004, *J Climate*, *19*(22), 5816-5842.

Altabet, M. A., et al. (1999), The nitrogen isotope biogeochemistry of sinking particles from the margin of the eastern North Pacific, *Deep-Sea Research*, *46*, 655-679.

Antonov, J. I., D. Seidov, T. P. Boyer, R. A. Locarnini, A. V. Mishonov, H. E. Garcia, O. K. Baranova, M. M. Zweng, and D. R. Johnson (2010), World Ocean Database 2009, in *NOAA Atlas NESDIS 66*, edited, US Govt Printing Office.

Brandes, J. A., and A. H. Devol (2002), A global marine fixed nitrogen isotopic budget: Implications for Holocene nitrogen cycling, *Global Biogeochemical Cycles*, *16*(4), 10.1029/2001GB001856.

Carton, J., and B. Giese (2008), A reanalysis of ocean climate using Simple Ocean Data Assimilation (SODA), *Mon Weather Rev*, *136*(8), 2999-3017.

Christensen, C. J., et al. (1994), Non-annual laminations and expansion of anoxic basin-floor conditions in Santa Monica Basin, California Borderland, over the past four centuries, *Mar Geol*, *116*(3,Äì4), 399-418.

Deutsch, C., et al. (2006), Physical-biological interactions in North Pacific oxygen variability, *J Geophys Res-Oceans*, *111*(C9), 1-16.

DeVries, T., et al. (2012), Global rates of water-column denitrification derived from nitrogen gas measurements *Nature Geoscience*(doi:10.1038/ngeo1515).

Garcia, H., et al. (2006), World Ocean Atlas 2005, Volume 3: Dissolved Oxygen, Apparent Oxygen Utilization, and Oxygen Saturation., in *NOAA Atlas NESDIS* edited, U.S. Government Printing Office, Washington, D.C.

Kritee, K., et al. (2012), Reduced isotope fractionation by denitrification under conditions relevant to the ocean, *Geochim Cosmochim Ac*(0).

Large, W. G., and S. Yeager (2004), Diurnal to decadal global forcing for ocean and sea-ice models: the data sets and flux climatologies., edited, NCAR Technical Note

Levitus, S., et al. (2009), Global ocean heat content 1955-2008 in light of recently revealed instrumentation problems, *Geophys Res Lett*, *36*, -.

Middelburg, J. J., et al. (1996), Denitrification in marine sediments: A model study, *Global Biogeochemical Cycles*, *10*(4), 661-673.

Rayner, N. A., et al. (2003), Global analyses of sea surface temperature, sea ice, and night marine air temperature since the late nineteenth century, *J. Geophys. Res.-Atmos.*, *108*(D14).

Smith, T. M., et al. (2008), Improvements to NOAA's historical merged land-ocean surface temperature analysis (1880-2006), *J Climate*, *21*(10), 2283-2296.

van Geen, A., et al. (2003), On the preservation of laminated sediments along the western margin of North America, *Paleoceanography*, *18*(4), -.

Vecchi, G. A., et al. (2006), Weakening of tropical Pacific atmospheric circulation due to anthropogenic forcing, *Nature*, *441*(7089), 73-76.

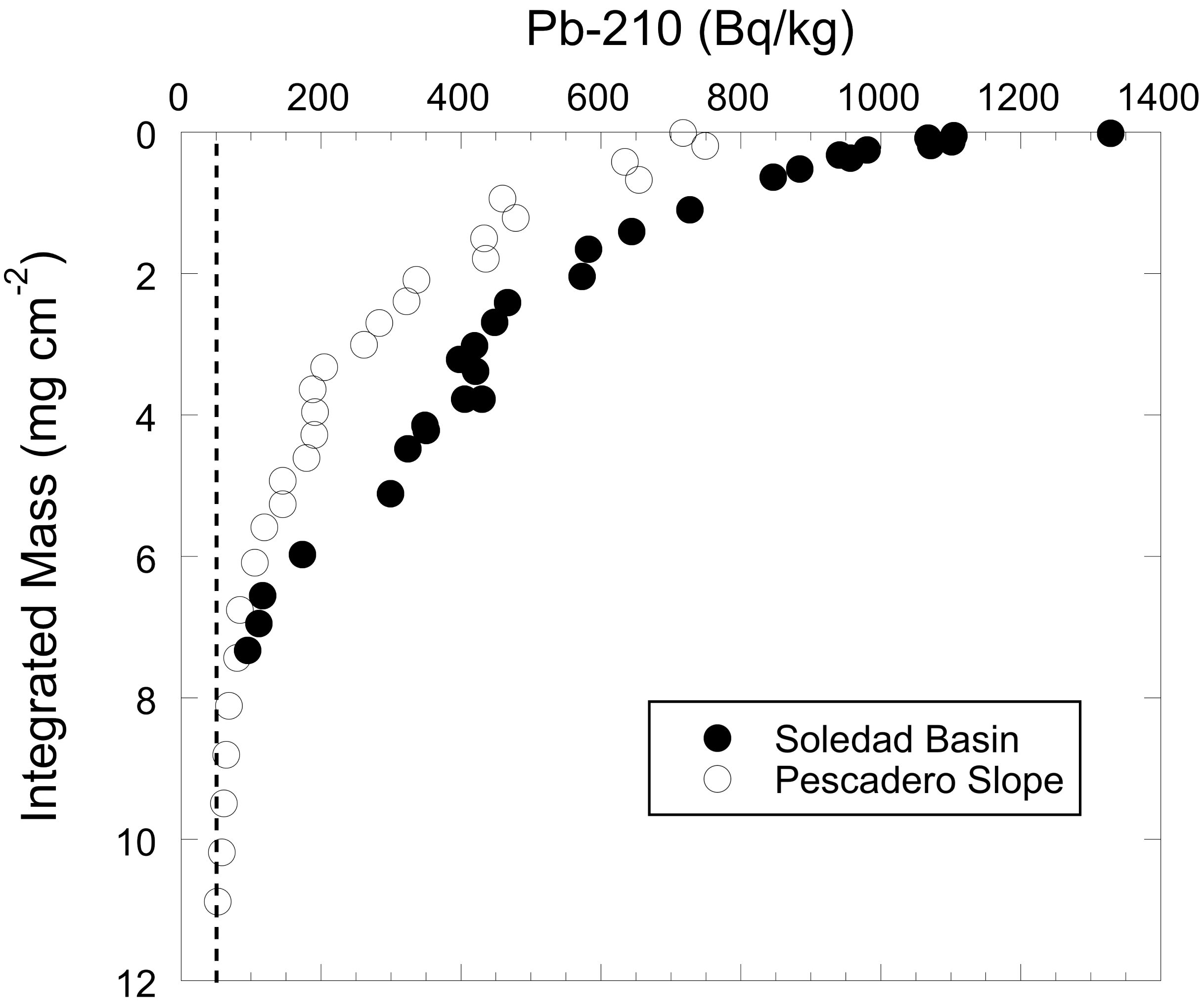

FIGURE S1

Excess ^{210}Pb as a function of cumulative mass at Pescadero Slope, and Soledad Basin.

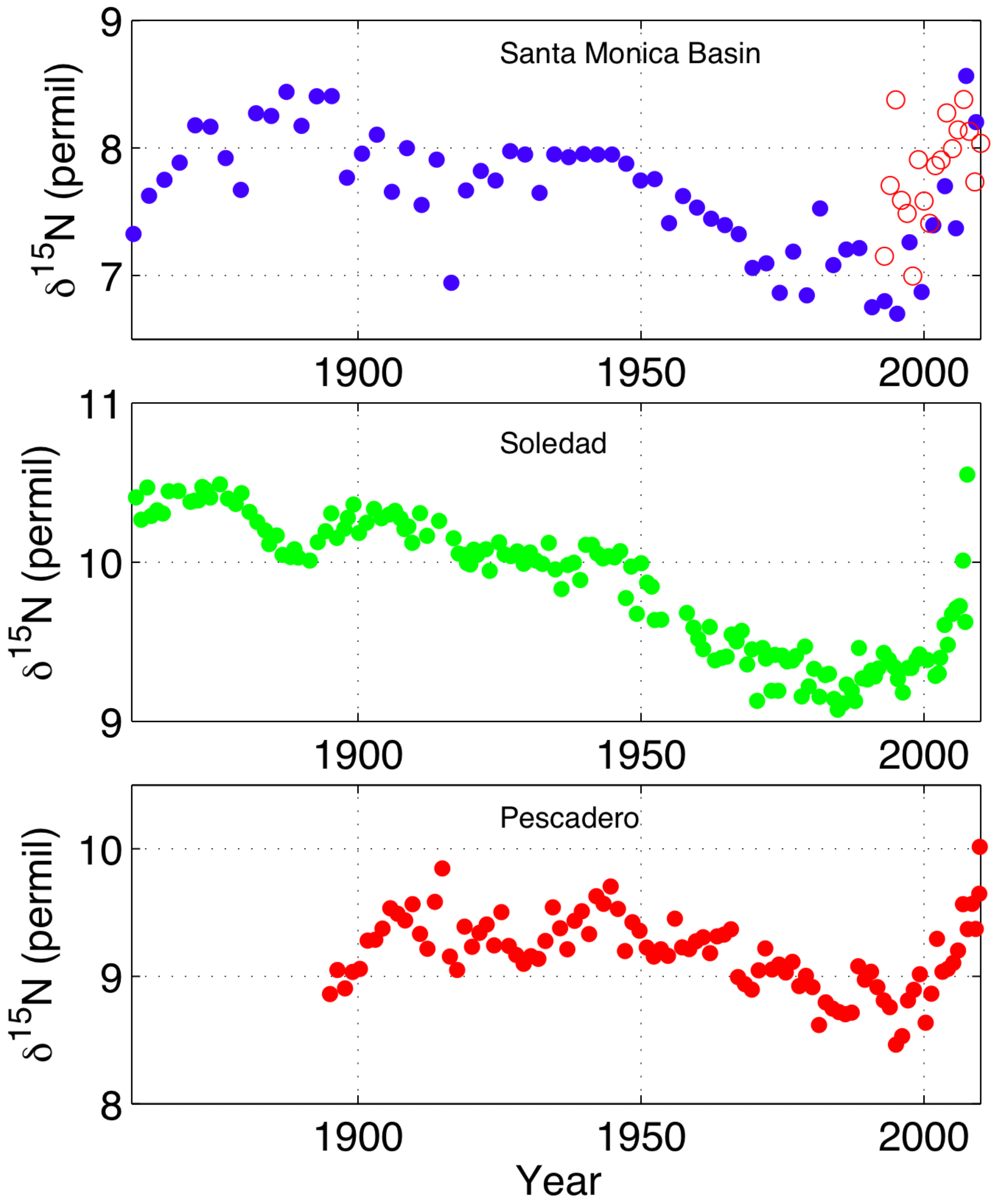

FIGURE S2

Sedimentary bulk organic $\delta^{15}N$ from 3 sites along the North American margin: A) Santa Monica Basin, B) Soledad, and C) Pescadero. Sediment records from Santa Monica Basin are overlaid by measured $\delta^{15}N$ of sinking particle flux from sediment traps deployed in the nearby Santa Barbara Basin from 1993-2010. Deviations from the long-term average at each site were used in Figure 1.

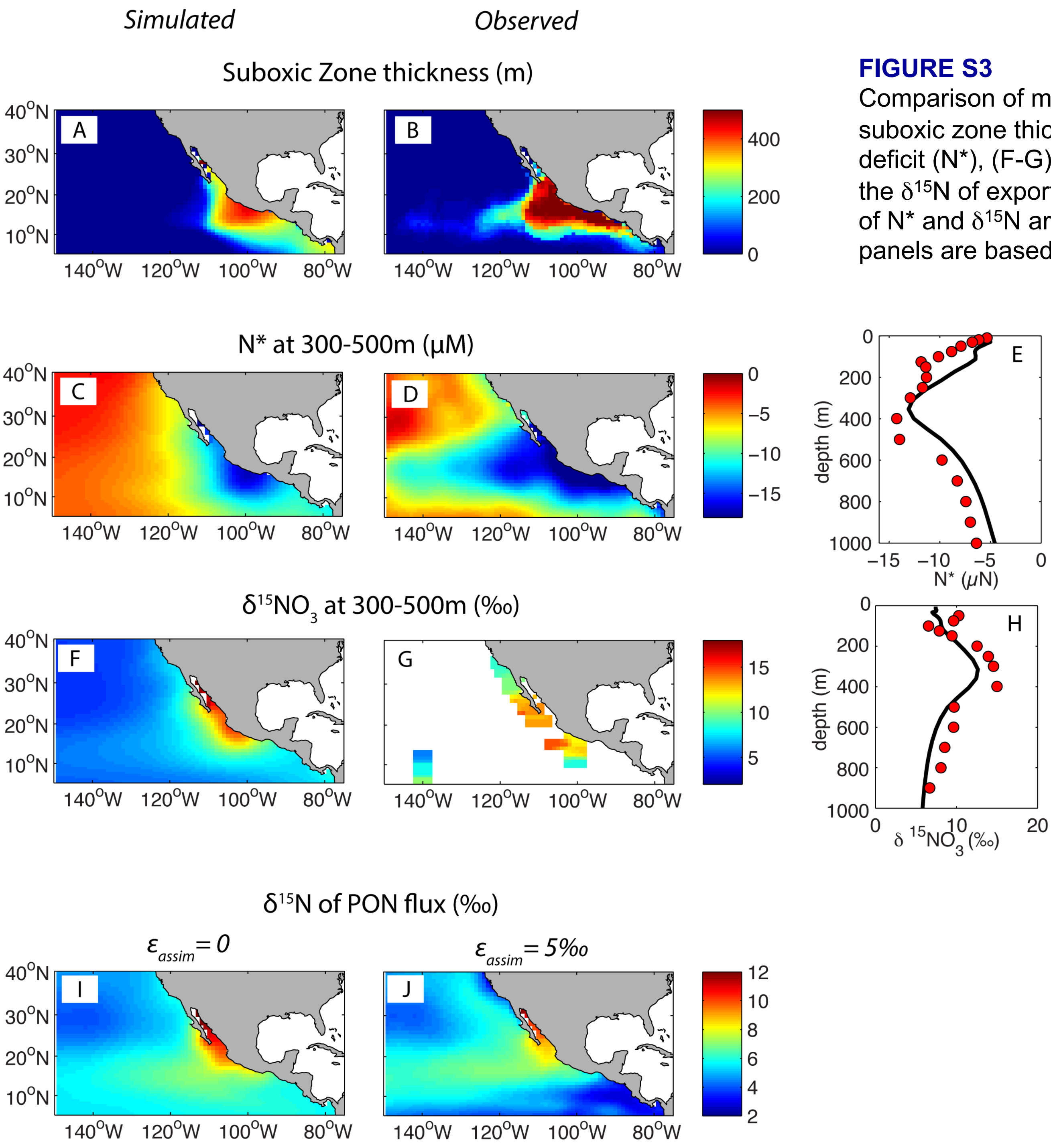

FIGURE S3

Comparison of model output to observations for (A-B) suboxic zone thickness, (C-D) the thermocline nitrate deficit (N*), (F-G) thermocline δ^{15}N of NO_3, and (I-J) the δ^{15}N of exported organic matter (bottom). Profiles of N* and δ^{15}N are also shown (E and H). Model panels are based on time-mean fields (1959-2005).

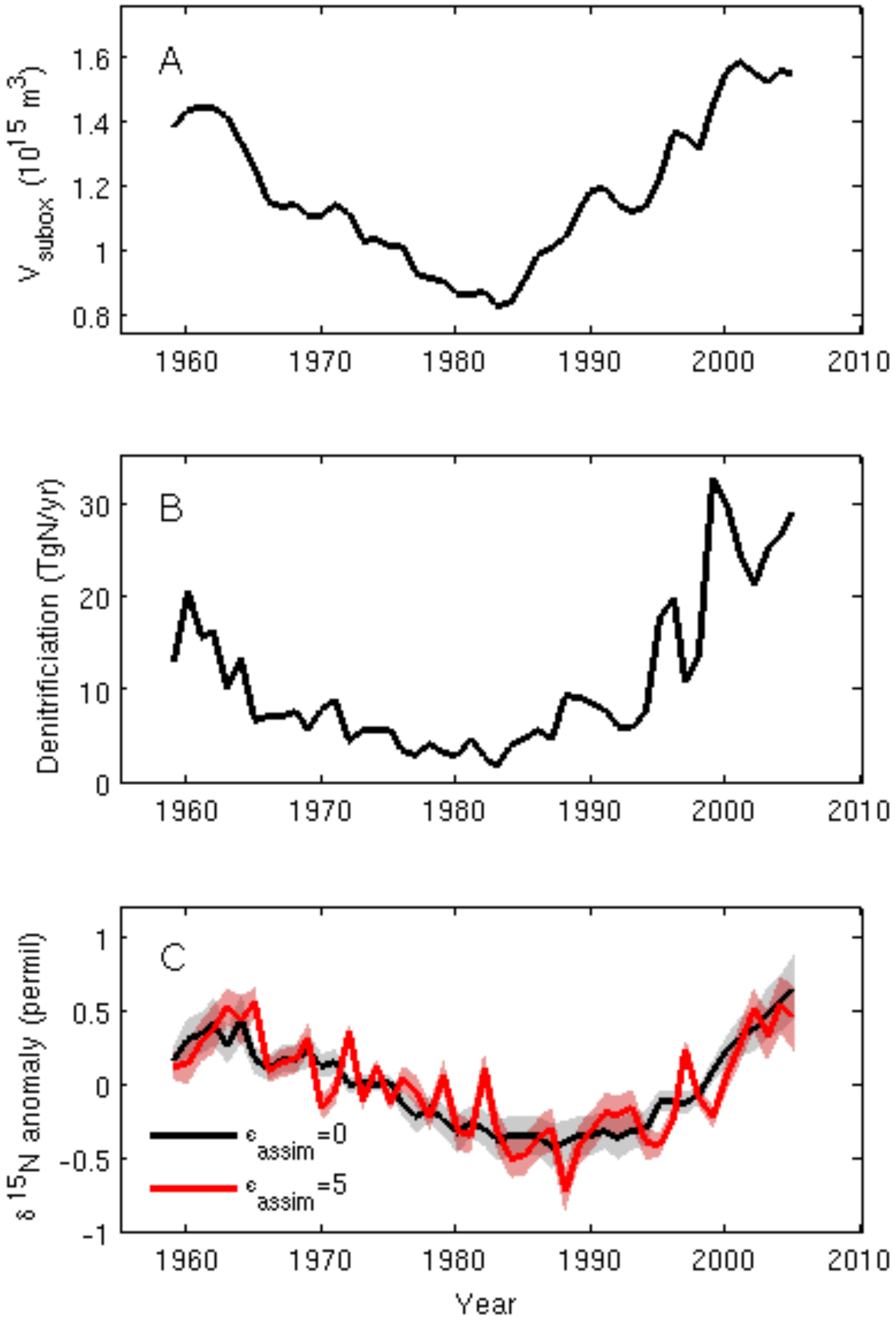

FIGURE S4

Time series of anoxic volume (A) and water column denitrification rate (B), and δ^{15}N of export flux (B) in N cycle hindcast model simulations. The isotope ratio of export is shown in cases with fractionation (red) and without (black). All quantities are integrated over the Eastern Tropical North Pacific.

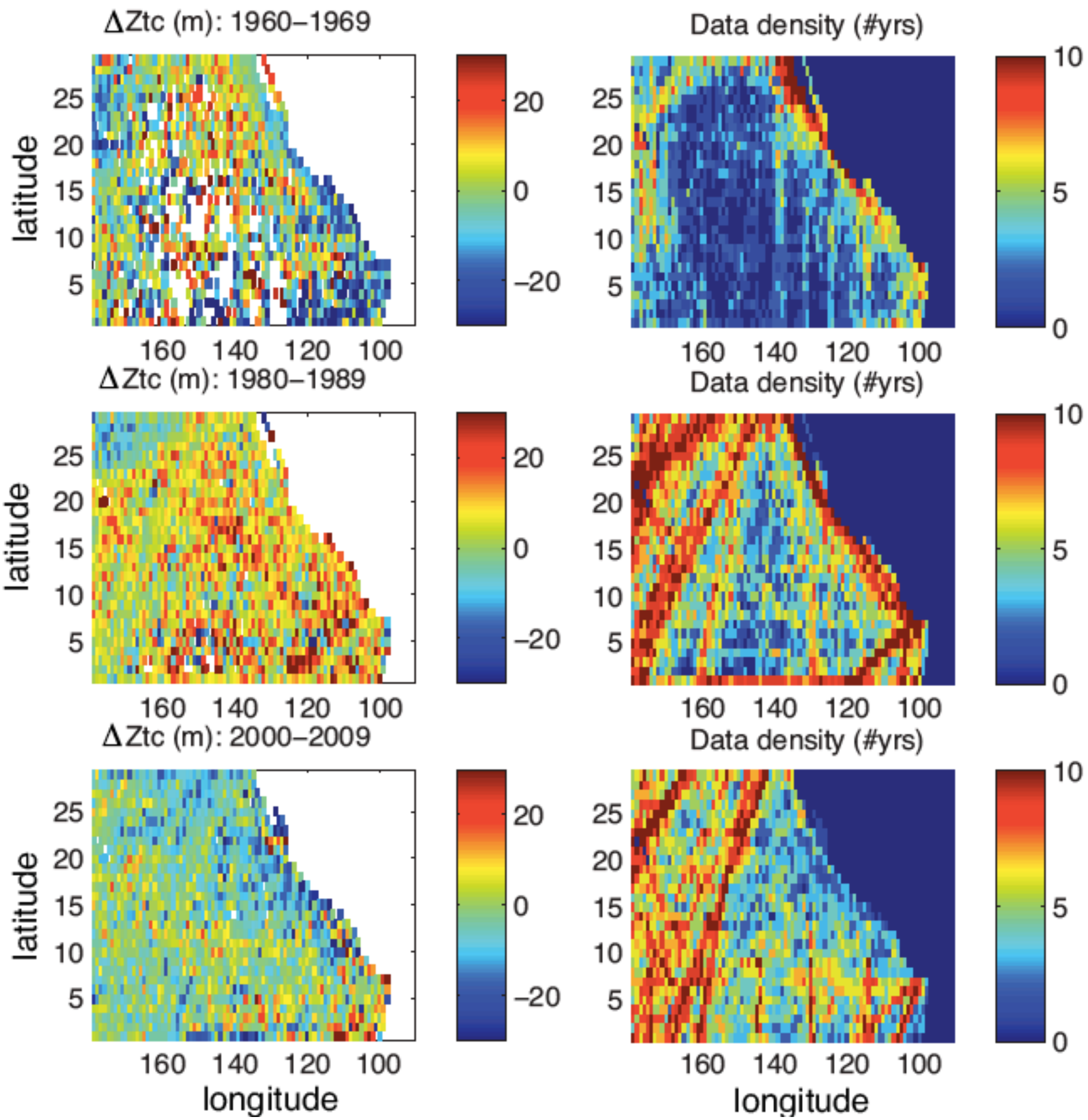

FIGURE S5

Decadal anomalies in thermocline depth, from 2009 World Ocean Database [ref]. The depth of the 13degC isotherm is taken as an index of the depth of suboxic water masses. It is estimated by linear interpolation of monthly mean temperature profiles on a 1° x 1° lat/lon grid. The data density is shown as the number of years in each decade for which at least one hydrocast exists. Temperature profiles are corrected for ocean heat uptake using CFC partial pressures, as described in SOM text.

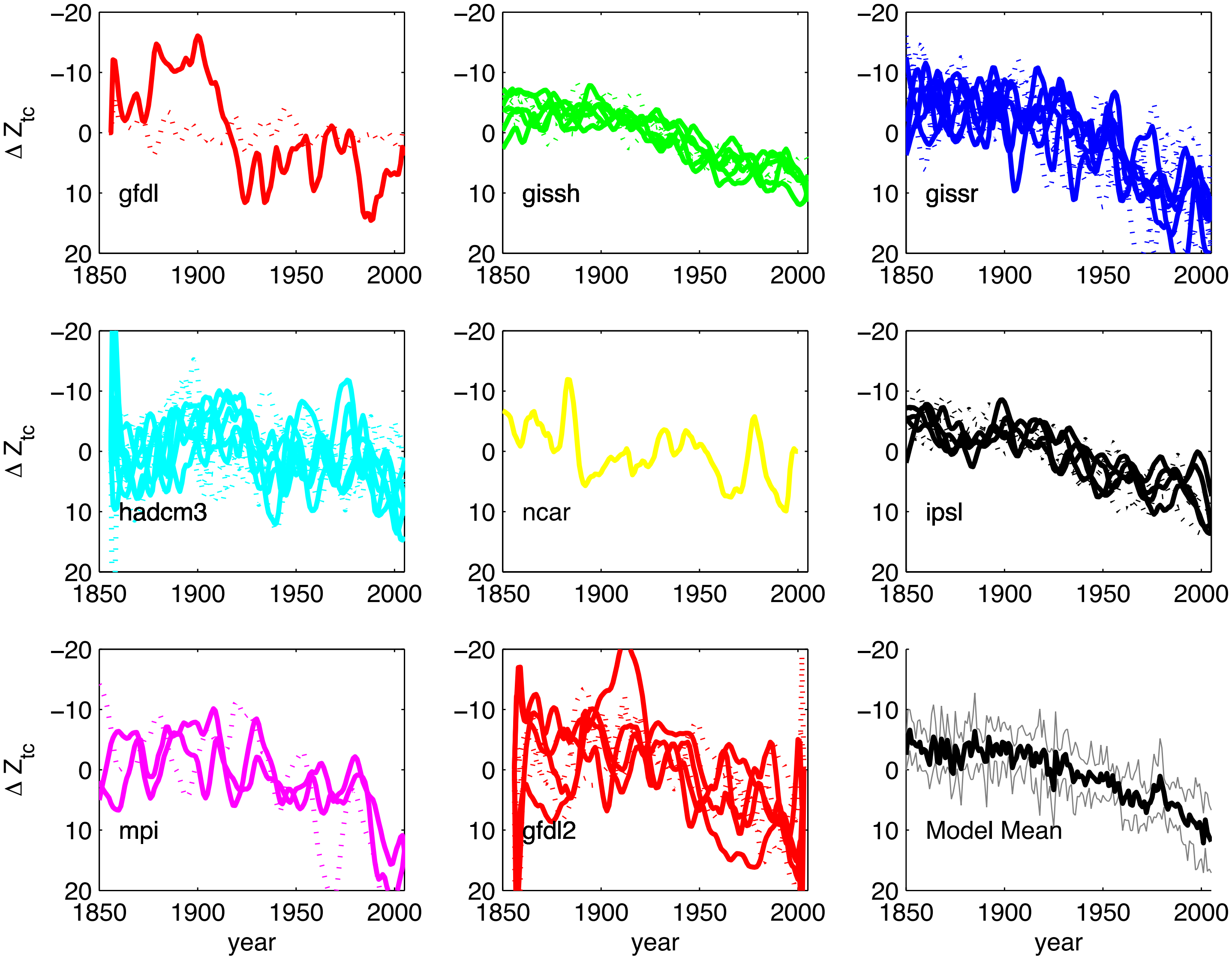

FIGURE S6

Trends in depth of 13ºC isotherm in the Eastern Tropical North Pacific, from coupled climate model output. Models runs are 20th century climate reconstructions from the IPCC AR4, and were run under historical radiative forcings, most importantly from greenhouse gases (GHGs). Trends in thermocline (13C isotherm) are the response to climate warming. Climate models without GHGs exhibit no deepening trend.

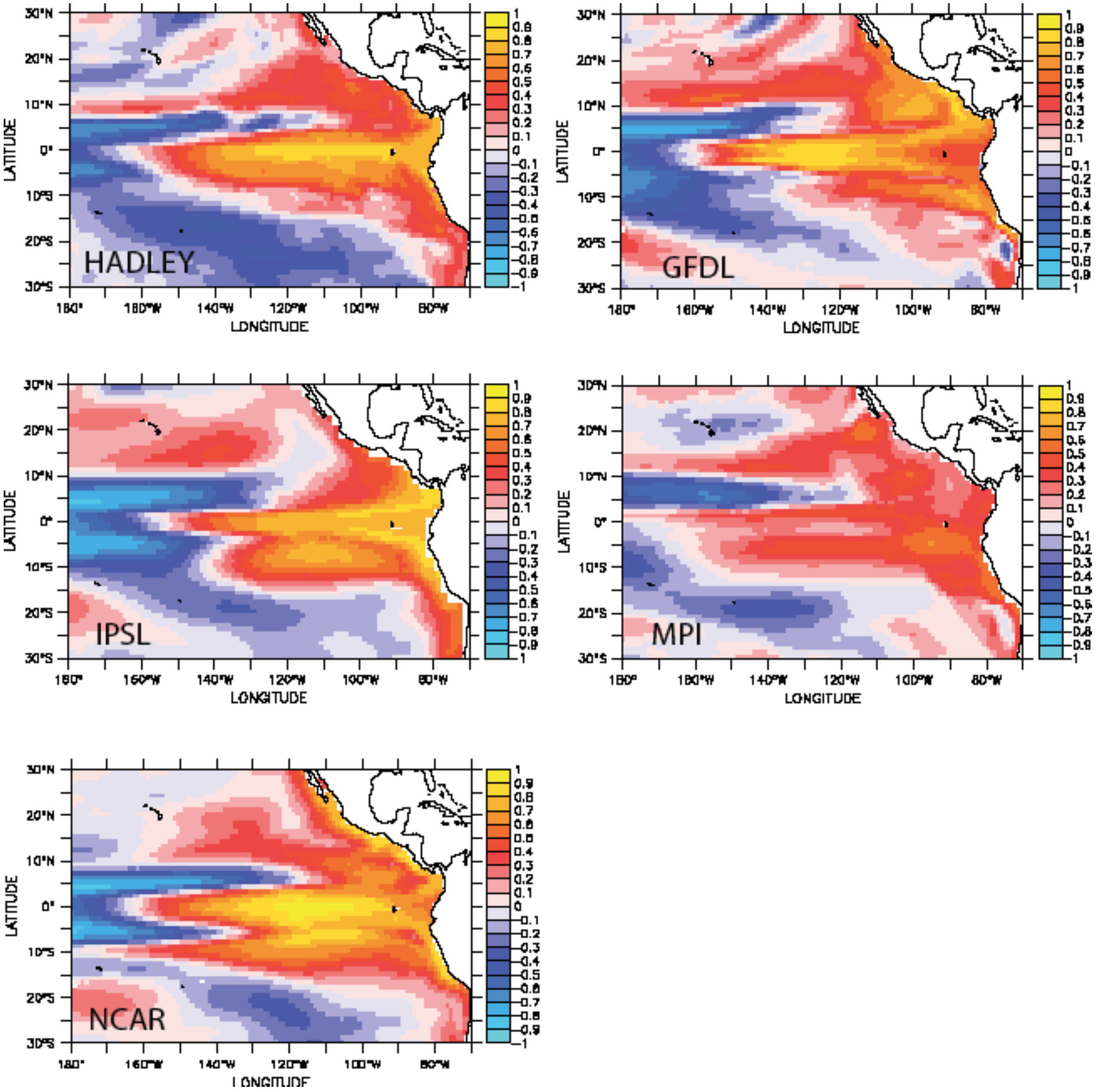

FIGURE S7
Correlation coefficient between equatorial wind stress and thermocline depth from 1850-2005, in Earth System Models. Annual wind stress is averaged over an equatorial band (3^{o}S-3^{o}N) in the central Pacific (160^{o}E-120^{o}W), and regressed against local changes in the depth of the 13^{o}C isotherm, which are smoothed with a 7-year boxcar average. Positive correlations indicate a deeper thermocline when winds are weaker.

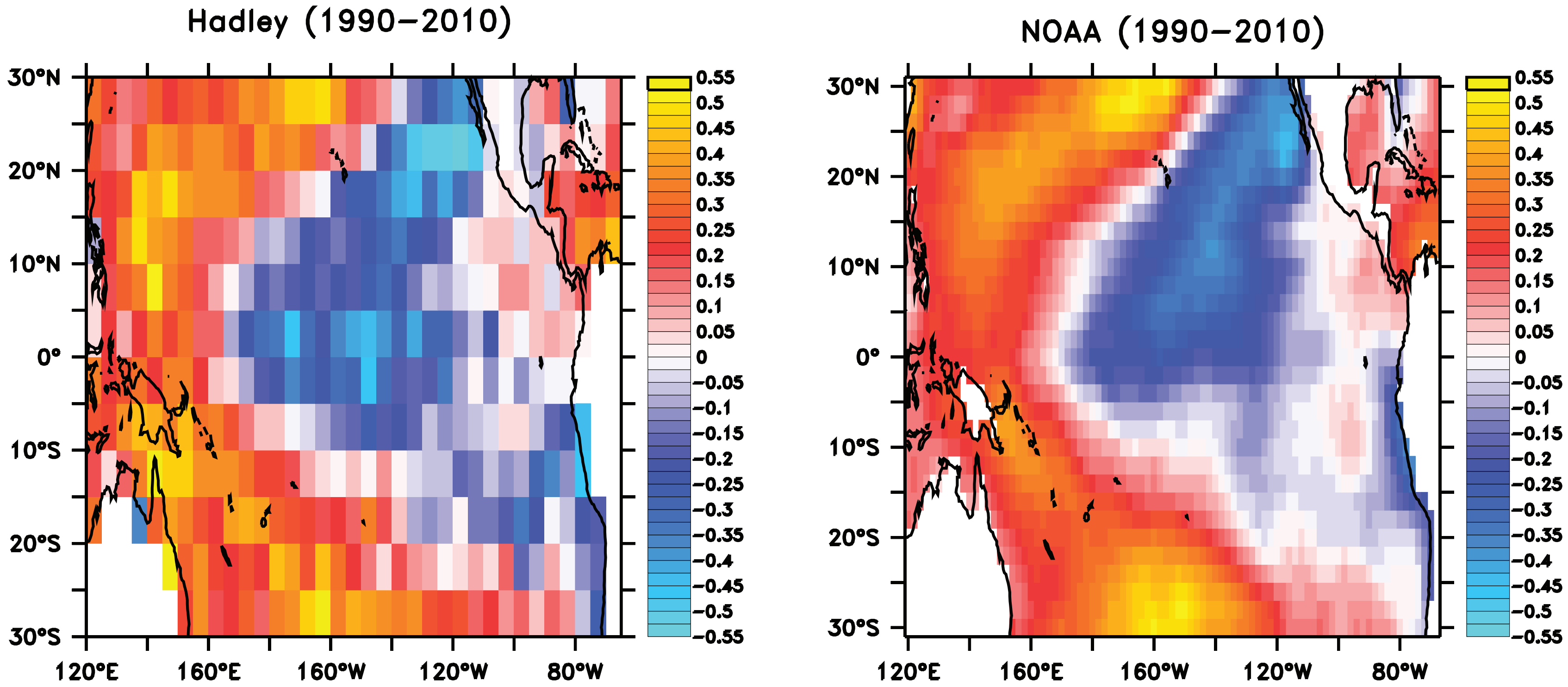

Hadley (1990–2010)

NOAA (1990–2010)

FIGURE S8

Trends in sea surface temperature from 1990-2010 in degrees C per decade. Trends are evaluated using monthly temperature anomalies at each grid cell. Two reconstructions of SST – Hadley center and NOAA's extended reconstructed SST product - show similar trend patterns. Over these decades during which anoxic zone has grown, cooling predominates in much of the eastern tropical Pacific, especially in the central equatorial Pacific where upwelling is most pronounced.